

# Combined magnetic resonance and bioluminescence imaging of live mice

## Mathieu Allard

Hospital for Sick Children  
Mouse Imaging Centre  
555 University Avenue  
Toronto, Ontario M5G 1X8  
Canada  
E-mail: mallard@sickkids.ca

## Daniel Côté

Université Laval  
Département de Physique  
Québec, Québec G1J 2G3  
Canada

## Lorinda Davidson

## Jun Dazai

## R. Mark Henkelman

Mouse Imaging Centre  
555 University Avenue  
Toronto, Ontario M5G 1X8  
Canada

**Abstract.** We perform combined magnetic resonance and bioluminescence imaging of live mice for the purpose of improving the accuracy of bioluminescence tomography. The imaging is performed on three live nude mice in which tritium-powered light sources are surgically implanted. High-resolution magnetic resonance images and multispectral, multiview bioluminescence images are acquired in the same session. An anatomical model is constructed by segmenting the magnetic resonance images for all major tissues. The model is subsequently registered with nonlinear transformations to the 3-D light exitance (exiting intensity) surface map generated from the luminescence images. A Monte Carlo algorithm, along with a set of tissue optical properties obtained from *in vivo* measurements, is used to solve the forward problem. The measured and simulated light exitance images are found to differ by a factor of up to 2. The greatest cause of this moderate discrepancy is traced to the small errors in source positioning, and to a lesser extent to the optical properties used for the tissues. Discarding the anatomy and using a homogeneous model leads to a marginally worse agreement between the simulated and measured data. © 2007 Society of Photo-Optical Instrumentation Engineers. [DOI: 10.1117/1.2745298]

Keywords: bioluminescence imaging; tomography; tissue properties.

Paper 06270R received Sep. 27, 2006; revised manuscript received Jan. 11, 2007; accepted for publication Feb. 2, 2007; published online May 31, 2007.

## 1 Introduction

Molecular imaging is concerned with detecting, localizing, and quantifying specific biomolecular processes in living cells.<sup>1-3</sup> Many uses have been proposed and demonstrated, such as tracking of specific cells, cancerous or not,<sup>4-7</sup> and observation of patterns of gene expression.<sup>8-10</sup> Among all the imaging modalities that are used for molecular imaging, optical techniques stand out because of the inherent ease of use, safety, and low cost. Optical imaging can be accomplished either with fluorescence, using fluorescent proteins [green fluorescent protein (GFP) and its variants] or exogenous probes,<sup>11</sup> or with bioluminescence, for which luciferases produce light.<sup>4</sup> In this paper, we focus exclusively on bioluminescence imaging.

There has been much effort lately devoted to transforming bioluminescence imaging from a 2-D, planar imaging technique into a truly 3-D tomographic imaging modality applicable to small animals.<sup>12-18</sup> A parallel effort has been carried out with fluorescence imaging.<sup>7,11,19</sup> The steps needed to realize bioluminescence tomography are, first, to acquire 2-D bioluminescence images (possibly multispectral) from different views and to generate a map of the light exitance (the intensity of the light exiting the body) on the animal skin; second, to generate an anatomical model of the animal from indepen-

dently acquired tomographic images and to register it with the optical images; third, to solve the forward problem, that is, to compute the light exitance map given the anatomical model and a volumetric distribution of the source of bioluminescence; fourth, to solve the inverse problem, that is, to find the source distribution that minimizes the difference between the computed and measured exitance maps. The first two steps offer many challenges of their own, and some researchers have devoted extensive efforts in constructing elaborate anatomical models.<sup>20,21</sup> However, most of the research has been focused on the forward and inverse problems.

The forward problem can be solved using Monte Carlo simulations,<sup>22,23</sup> finite-element methods,<sup>24,25</sup> or analytical methods (approximate or perturbative) based on Green's function.<sup>12,13,18</sup> All of them have in common that they operate on an anatomical model consisting of the union of several regions corresponding to different tissues in the animal. When building such a model, one must assign an absorption coefficient and a reduced scattering coefficient to each tissue. These values should be measured independently of the bioluminescence imaging experiment. How accurate bioluminescence tomography can be as an imaging modality therefore critically depends on how the chosen values for the optical properties are representative of the true properties of the tissues. Obtaining accurate optical tissue properties is quite challenging, however. First, measurements of absorption and scattering coefficients are notoriously difficult to accomplish.<sup>26-29</sup> Most

Address all correspondence to Mathieu Allard, Hospital for Sick Children, Mouse Imaging Centre, 555 University Avenue, Toronto, Ontario M5G 1X8 Canada. Tel: 416-813-2202; Fax: 416-813-2208; E-mail: mallard@sickkids.ca

published values were measured on fixed or frozen tissue samples and may not be representative of the *in vivo* properties of tissues. Second, even properties measured *in vivo* on one animal may not be accurate when applied to another animal of another age, strain, or disease state. Third, the validity of the implicit assumption that the optical properties are homogeneous within a given organ or tissue is open to questioning, especially in organs with obvious heterogeneity such as kidneys and gut.

Several algorithms that can solve the inverse problems have been described in recent published work.<sup>15–18,30–32</sup> Generally, numerical or experimental phantoms are used to test the accuracy of the algorithms. The phantoms have well-characterized optical properties, and the three problems just described do not arise.

In this paper, we present a methodology to acquire and coregister magnetic resonance imaging (MRI) and bioluminescence imaging (BLI) images on live mice. From MRI images, we constructed an anatomical model and solve the forward problem of bioluminescence tomography. Our main goal is to investigate how accurately the forward problem can be solved in a real mouse. Another objective is to evaluate how much a detailed anatomical model contributes to the accuracy of the solution, and whether bioluminescence tomography is feasible without. We believe that the accuracy of the anatomical models and of the tissue optical properties in this paper is as good as it can be, given the restrictions imposed by working with live mice. We expect that our findings will be applicable to real bioluminescence imaging experiments for pre-clinical studies.

The experiments on which we report here consisted of implanting artificial light sources at known locations in live mice, and performing combined MRI and BLI. Strictly speaking, this is not bioluminescence, however, we will keep the BLI acronym for clarity. The anatomical model was created by segmenting the MRI images. The optical properties, obtained from collaborators, were measured *in vivo* directly on the organs of a live mouse with a multifiber probe. Simulated exitance maps, obtained with a Monte Carlo algorithm, were then directly compared to the measured data. To ensure that the findings are applicable to bioluminescence sources located in various tissues, we performed identical experiments on three mice, with the artificial sources implanted at three different locations.

We chose to focus exclusively on the forward problem, and have not attempted to reconstruct bioluminescence images, even though reconstruction of images is the end-goal of bioluminescence tomography. Although the progress has been rapid in this field, the algorithms for solving the inverse problems are known to introduce errors, which could complicate the interpretation of the results presented here.

This paper is structured as follows. Section 2, describes how the magnetic resonance and luminescence measurements were carried out. The construction of the anatomical models and the simulations of the propagation of light in the mice is presented in Sec. 3. Section 4 presents the simulated and the measured light exitance maps, and quantifies the agreement between the two. We discuss the implications of our results in Sec. 5, and conclude the article.

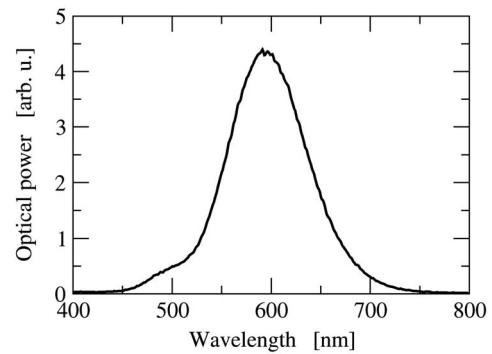


**Fig. 1** Spectrum of the light emitted by the tritium-powered light source (Traser) implanted in the mice.

## 2 Experiment

CD1-Nude mice (Charles River Labs, Wilmington, Massachusetts) were used as animal models since hair interferes with optical measurements. The experiments were performed on three female mice, aged from 3 to 9 months and weighing from 24 to 28 g. All animal protocols were approved by the Animal Care Committee of the Hospital for Sick Children, which is subject to the Canadian Council on Animal Care regulations.

To simulate bioluminescent sources, we surgically implanted Trasers from MB-Microtec (Bern, Switzerland) in three live nude mice. These permanent light sources are cylindrical glass vessels (0.9 mm in diameter, 2.5 mm in length) internally coated with an orange phosphor and filled with tritium gas. The total light output from the Trasers was typically  $2.0 \times 10^8$  photons/s, or about 6.6 pW. We measured the spectrum of the light emitted by the Traser; it is shown in Fig. 1. In the first nude mouse (henceforth called mouse 1), a Traser was glued to the left kidney capsule with Vetbond from 3M. In the second mouse (mouse 2), a Traser was glued to a liver lobe near the gall bladder. In the third mouse (mouse 3), a Traser was glued to the outer wall of the small intestine. The wounds were allowed to heal for at least 1 week before imaging was performed. The implantation of the Trasers did not appear to have any lasting impact on the health of the mice.

The MRI was performed with a 7-T Inova scanner from Varian (Palo Alto, California, USA). The BLI was performed with an IVIS-3D prototype system from Xenogen (Alameda, California, USA), which is capable of acquiring luminescence images at multiple wavelengths and from multiple views and to produce 3-D images of the animal. To enable sequential MRI and BLI while the mouse remained in the same posture, we built a MRI-compatible platform that could be used in both instruments (see Fig. 2). For MRI, the platform is integrated in a larger setup that comprises an rf coil, delivery and scavenging systems for the anesthetic gas, a warm-air heating system, and monitors for respiration, heart rate and temperature.

To maximize the signal-to-noise ratio (SNR) in the MRI images, we custom-designed and built a modified birdcage coil, 5 cm in diameter and 15 cm long. The dimensions were selected to enable the mouse to be imaged with stretched limbs; this is preferable for BLI. Since the platform was

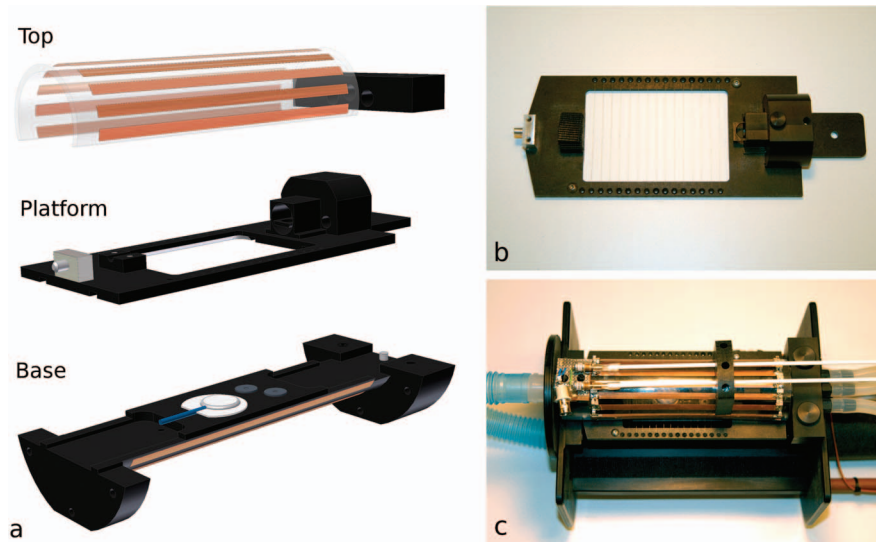


**Fig. 2** (a) Exploded computer drawing of the platform on which the MRI and the BLI were performed. The setup comprises three independent parts: first, the top piece of the rf coil; second, the platform itself (which comprises the anesthetic gas inlet); third, the supporting base, which incorporates the heating, monitoring systems and the bottom piece of the rf coil. All three parts are used in the MRI scan, while only the platform is used in the BLI scan. (b) Photograph of the platform alone; the mouse is supported by a net made of a fine nylon filament, and held in place by a bite bar and a tail restraint. (c) Photograph of the assembled platform. The pipe on the left brings warm air; the ones on the right deliver the anesthetic gas and connects to the scavenging pump. The white rods are used to tune and match the rf coil.

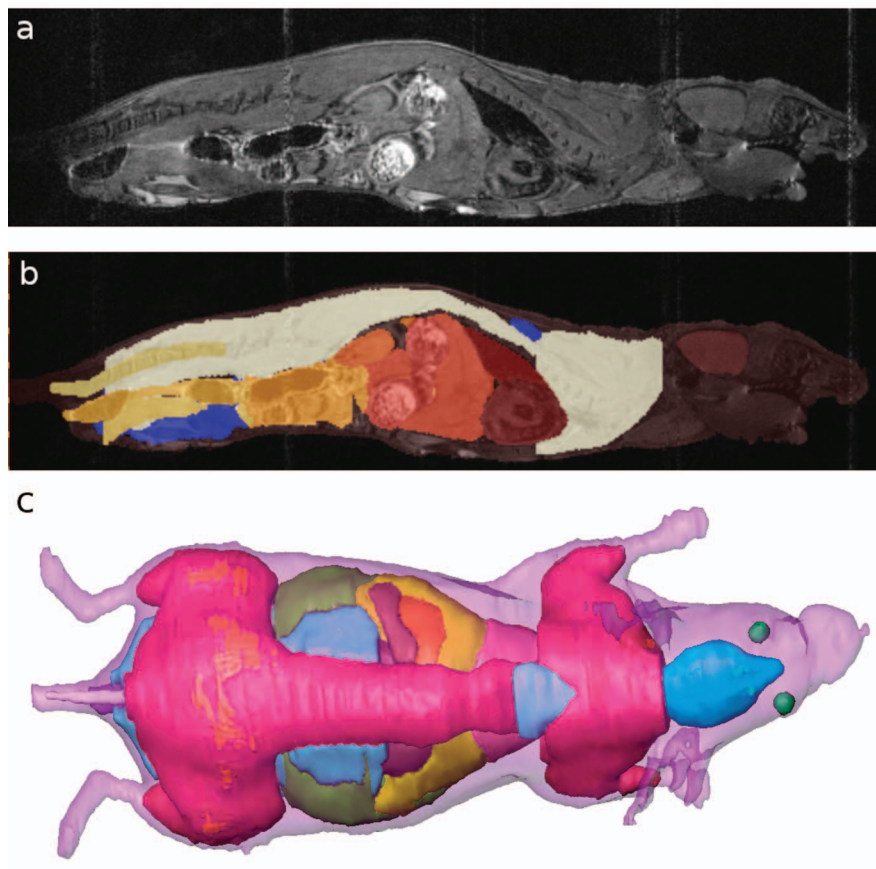


**Fig. 3** (a) Magnetic resonance image of mouse 3 (sagittal slice); (b) same slice as (a), where the different tissues have been colored and the labeled tissues are listed in the text, and (c) 3-D dorsal view of the segmented tissues.

8.5 cm wide, the coil was split into two asymmetric parts (above and below the platform) that were inductively coupled. The capacitors in the coil end-rings were individually selected to balance the current in the rungs. Standard MRI tests showed that the coil had a quality factor  $Q$  of 60 when loaded.

The MRI images were acquired with a 3-D fast spin-echo sequence. The scan parameters were echo time (TE) = 7.1 ms (effective), repetition time (TR)  $\approx$  300 ms, isotropic resolution of 0.208 mm, field of view of  $25 \times 37 \times 100 \text{ mm}^3$ , six echos, and four averages. The field of view covered the entire mouse. Prospective gating was used for both the respiration and the heart rate to ensure that the acquisition was all done during the quiescent part of the breathing cycle and at the same point of the cardiac cycle. The TR was selected to be two heartbeats. The total imaging time was approximately 120 min. No contrast agent was used. The mouse was maintained under anesthesia with isoflurane during the scan. The image contrast was characteristic of the first echo and the average SNR was 23.

The BLI images were acquired immediately after the MRI was complete. During the transfer between the two instruments, the mouse remained under anesthesia and in the same posture. Luminescence images were acquired in eight views (45 deg apart), at three different wavelengths (580, 620, and 640 nm), and for 3 min each. The IVIS-3D system uses a structured illumination system to reconstruct the 3-D surface of the mouse.<sup>15</sup> The luminescence images are then projected on this surface to create an intensity map on the skin of the mouse. The IVIS-3D can compute an approximate volume reconstruction of the distribution of the luminescence source.<sup>15</sup> This algorithm does not take into account the anatomy of the mouse, however, and was not used in this study.

### 3 Model

Before the propagation of light from the source to the skin could be simulated with the Monte Carlo algorithm, the following steps had to be taken: registration of BLI and MRI images to each other, segmentation of MRI images, and generation of surfaces defining the interfaces between tissues. These steps were performed independently on all three mice.

The MRI and BLI images were first aligned manually using the 3-D visualization software AMIRA from Mercury Computer Systems (San Diego, California, USA). The MRI image was rotated (along three axes) and translated (along three axes) until the skin in both images coincided. No scaling was applied since both instruments are absolutely calibrated in millimeters. The BLI and MRI images were both cropped in the rostral-caudal direction to the abdominal region, where luminescence was detected. Because the MRI and BLI images were acquired with the mouse in the same posture, the location of the body surface generally coincided in the two images. To remove any residual differences, the two images were registered automatically with a nonlinear transformation. This was accomplished with the MINCTRACC program, distributed by the Montreal Neurological Institute of the McGill University.<sup>33,34</sup> The algorithm searched for the transformation that maximized the cross-correlation between the binary interior-exterior images generated from the MRI and BLI im-

ages. We selected for the algorithm a blurring kernel of 1 mm and a stiffness parameter of 0.99.

The registered MRI image was then manually segmented for all major tissues with AMIRA. The following tissues were identified in the mouse abdomen: heart, lungs, liver, stomach, small intestines, colon, kidneys, spleen, bladder, uterus, muscle, fat, bones, and spine. As it is difficult to differentiate the intestines from the pancreas and other conjunctive tissues in the MRI image, all of these were considered part of the same tissue. The few remaining unlabeled voxels (mostly in the skin, conjunctive tissue, and small muscles) were considered to be part of a single tissue group. Following the segmentation, the volume data was transformed into a series of surfaces that defined the interfaces between the tissues, again with AMIRA. The surfaces consisted of closed meshes of triangles. The surfaces were then automatically simplified to reduce the total number of triangles to approximately 25,000 for all interfaces combined.

The optical properties for each segmented tissue [absorption coefficient  $\mu_a$  and reduced scattering coefficient  $\mu'_s = (1-g)\mu_s$ ] were provided by (and are proprietary to) Xenogen. For all tissues considered here,  $\mu_a$  ranged from 4.4 to 41  $\text{cm}^{-1}$  at 580 nm and from 0.35 to 3.2  $\text{cm}^{-1}$  at 640 nm. Values of  $\mu'_s$  ranged from 4.5 to 45  $\text{cm}^{-1}$ , with little dependence on wavelength. The refractive index was taken to be 1.4 for all tissues.<sup>28</sup> The optical properties were measured *in vivo* with optical fiber probes.<sup>29,35</sup>

The position of the Trasers was determined directly from the MRI images, where they appear as dark cylinders. The optical power (at each wavelength) of the bare Trasers was measured with the IVIS-3D systems prior to their implantation in the mice.

The optical simulations were carried out with the POLMC software,<sup>36</sup> which employs a standard Monte Carlo algorithm to generate paths of photons from the source to the skin of the mouse. In each simulation,  $10^7$  photons paths were generated, which was large enough to effectively eliminate statistical noise. The algorithm was implemented with isotropic scattering, that is, with  $g=0$  and  $\mu_s = \mu'_s$ . For each mouse, the simulation was carried once for each wavelength (580, 620, and 640 nm). The simulation was then run twice again at 620 nm using a homogeneous medium for the entire body; we used, first, the optical properties of muscle (the largest tissue group), and second, the properties of the tissue surrounding the Traser (liver or intestines). Each simulation took of the order of 8 h to run on a personal computer.

### 4 Results

Magnetic resonance images were acquired under the same conditions on all three mice. A sagittal slice from the MRI image of mouse 3 is shown in Fig. 3, along with an image showing the labels in the same slice. In the same figure we also show a 3-D view of the tissue interfaces, which by themselves alone constitute the anatomical model. Apart from small postural differences, there are no striking differences between the images of the three mice.

The BLI images are shown in Fig. 4. The planar ventral view of mouse 3 clearly shows the illumination spot due to the Traser glued to the outer intestinal wall. The 3-D views provide a better overall picture, however. The spots due to the

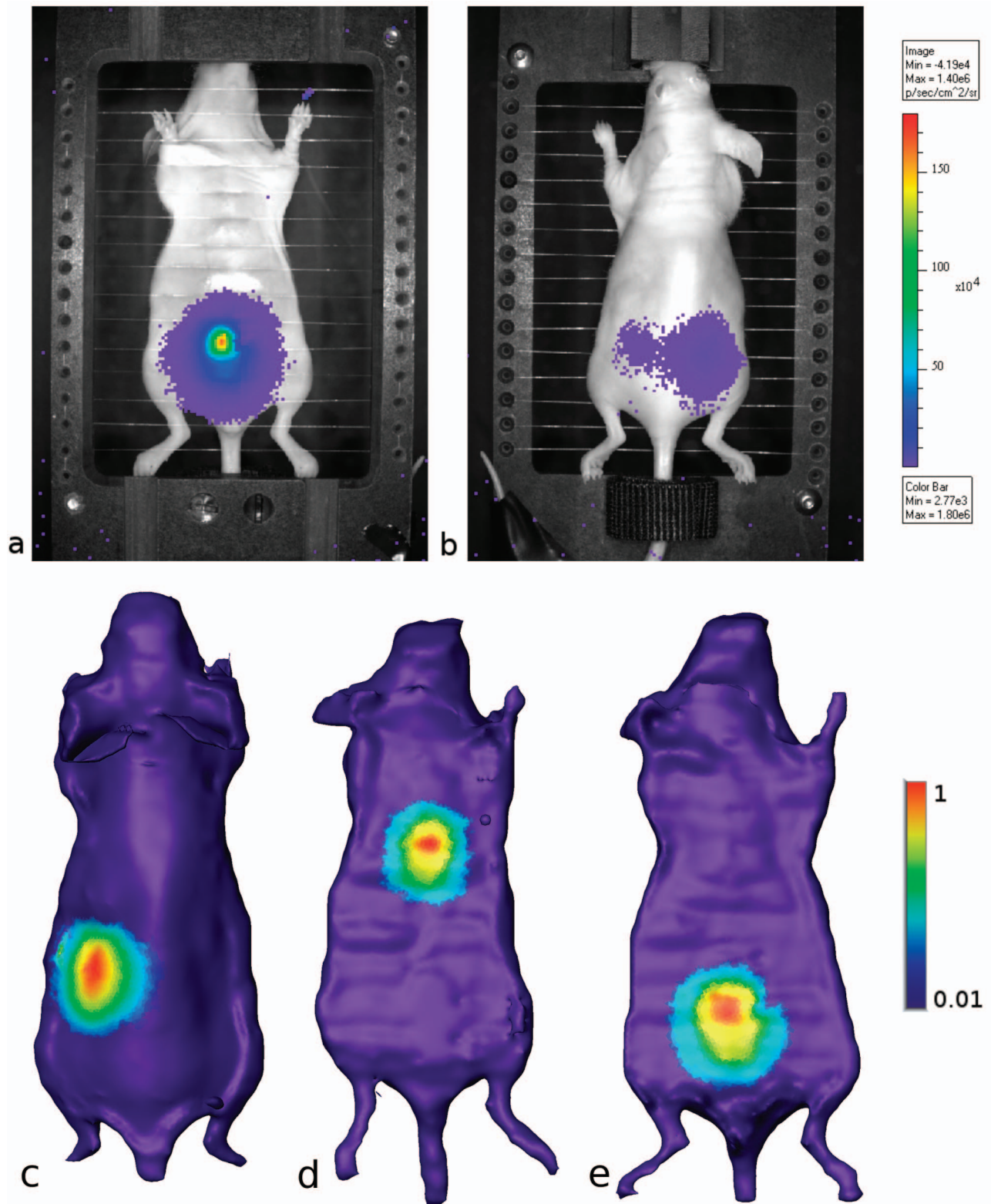


**Fig. 4** (a) Ventral view of mouse 3. This is a color-coded luminescence image (taken at 620 nm) superimposed on a black and white photograph. (b) Dorsal view of mouse 3. Images in (a) and (b) are shown on the same color scale. (c) 3-D dorsal view of mouse 1; the luminescence is denoted by a logarithmic color scale, normalized to the peak exitance and covering two orders of magnitude in brightness. (d) Same, with mouse 2 (ventral view). (e) Same, with mouse 3 (ventral view).

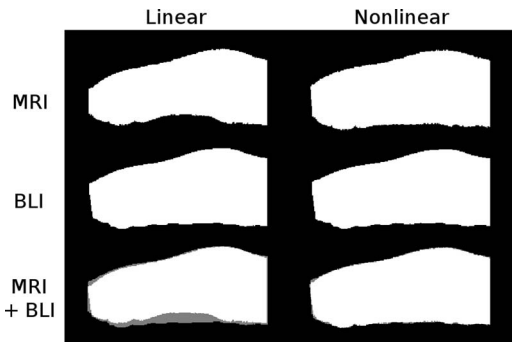


**Fig. 5** Left: binary MRI (top) and BLI (middle) images (sagittal slice) of mouse 3, with the interior shown in white and the exterior in black, after they were linearly coregistered. The image at the bottom is a superposition of the other two, with gray areas denoting where they do not coincide. Right: Same slice, after the nonlinear automatic registration step. The gray areas have almost disappeared.

Traser glued to the left kidney (for mouse 1) and the one implanted in the liver (for mouse 2) are clearly visible. Within the imaging conditions selected, no luminescence other than that of the Traser could be detected; in other words, there is no detectable autoluminescence. Instrument noise is the only source of background signal, and was eliminated by applying a suitable threshold to the data ( $2700 \text{ photons s}^{-1} \text{ cm}^{-2} \text{ sr}^{-1}$ , or 0.14% of the peak luminescence, in Figs. 4(a) and 4(b)) before reconstructing the surface luminescence images.

As explained in Sec. 3, the MRI images (along with the tissue labels) were registered in two steps to the surfaces created from the luminescence imaging software. Figure 5 shows the accuracy of the registration, after the first (manual and linear) step and after the second (automatic and nonlinear) step. Over the midbody sagittal slice, the contours of the MRI and BLI images were at most 2.8 mm from each other after the first step. The largest distance was found where the mouse was resting on the raised respiration monitoring pad during the MRI; this pad was absent during the BLI. The second registration step successfully brought into coincidence the position of the skin in the two images: the contours were then at most 0.4 mm (2 voxels) of each other everywhere.

Monte Carlo simulations of the propagation of light were carried out on the registered anatomical models for all three mice. The computed light exitance patterns were then compared to the measured exitance patterns shown in Fig. 4. For mouse 3, the simulated and measured images are shown side by side (on the same intensity scale) in Fig. 6. The position of the illumination spot is the same in both images, and its spatial extent is slightly larger in the measured image. The peak intensity is also about 2.5 times greater in the measured image, although this is not obvious because of the logarithmic scale. Although the intensity scale was chosen to fit the range of exitance in the images, we emphasize that this is an absolute measurement. Integrating the exitance over the whole body surface shows that 5.3% of the light emitted by the Traser (2.1% in the simulation) escapes the mouse's body at 620 nm.

To provide a better and more quantitative measure of how close the measured and simulated data are, we compared relevant statistics on the two data sets. The peak exitance, the

fraction of the total emitted optical power exiting the mouse, and the area of the illumination spot (taken to be the region where the exitance exceeds half of its peak value) were computed for all three mice and are shown in Table 1. The distance between the exitance peak positions in the measured and simulated exitance images was also computed. These numbers were computed independently at all three wavelengths. These numerical measures enable an easier comparison of the simulated and measured data sets than the graphical images. Accordingly, to save space, we chose not to show the simulated images on mice 1 and 2, or those obtained at 580 and 640 nm.

To directly compare the measured and simulated data sets, the measured and simulated exitance patterns must first be mapped onto a common surface mesh. Although the meshes in the anatomical model and in the measured BLI image are defined on approximately the same surface, the locations of the vertices in the two meshes are independent. This was done with a linear 2-D interpolation scheme, where the position of the vertices above or below the surface was ignored. The mapping enabled us to compute a normalized root mean square (NRMS) difference between the two data sets, according to the following formula:

NRMS difference

$$= \left\{ \frac{\sum_i [(I_i^{\text{meas}} - I_i^{\text{sim}}) a_i]^2}{[\sum_i (I_i^{\text{meas}} a_i)^2]^{1/2} [\sum_i (I_i^{\text{sim}} a_i)^2]^{1/2}} \right\}^{1/2}, \quad (1)$$

where the sum is made over all triangles; and  $I_i^{\text{meas}}$  and  $I_i^{\text{sim}}$  are the measured and simulated intensity mapped to the same triangle  $i$ , of which  $a_i$  is the area.

The absorption of tissue is known to increase significantly below 600 nm, where hemoglobin absorbs strongly.<sup>28</sup> Accordingly, we find that the fraction of the emitted light that exits the body at 580 nm is at least one order of magnitude smaller than at 620 nm, both in the simulated and in the measured data. Another direct consequence of the increased absorption is the smaller illumination spots. There is, on the other hand, a much smaller difference between the 620- and 640-nm data sets.

A direct comparison of measured and simulated exitance shows different degrees of correspondence for the three Traser locations. The agreement is generally excellent for mouse 1 (Traser on kidney), for which the differences in peak and total exitance are less than 10%. The distance between the measured and simulated location of the peak exitance is small: 1.6 mm is about the length of the mesh triangles. This small difference is, however, large enough to cause a significant NRMS difference of 32%. This shows how sensitive the latter is to small differences in data sets. The agreement between simulation and measurement is not as good for mouse 2 (Traser in liver), for which the peak and total exitance differ by factors of about 4 and 2, respectively. Accordingly, the NRMS difference takes a very large value, over 100%. For mouse 3 (Traser in intestines), the peak and total exitance both differ by a factor of about 2.5. The origin and significance of these discrepancies are discussed in the next section.

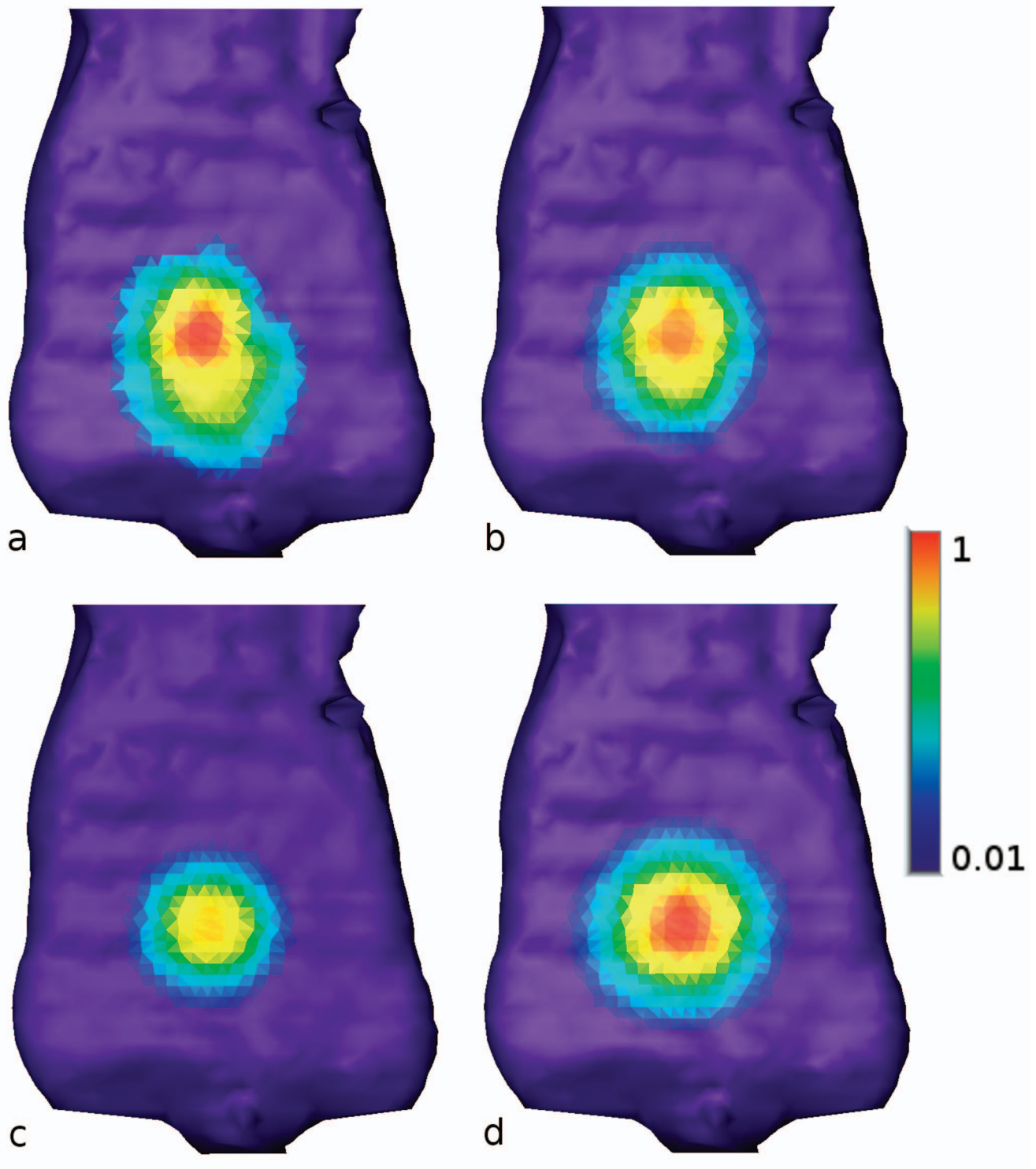


**Fig. 6** (a) Measured light exittance on mouse 3. (b-d) Simulated light exittance on mouse 3 (b) using heterogeneous optical properties, (c) using homogeneous optical properties equal to those of intestines, and (d) using homogeneous optical properties equal to those of muscles. The four images are shown on the same logarithmic color scale, normalized to the peak of image (a) and spanning two orders of magnitude.

**Table 1** Comparison of measurements and simulations.

Data set	Exitance		Spot Area (mm <sup>2</sup> )	Peak Distance (mm)	NRMS Difference (%)
	Peak (mm <sup>-2</sup> )	Total (—)			
Mouse 1: Traser on kidney					
580 nm					
Measured	$3.9 \times 10^{-5}$	$3.3 \times 10^{-4}$	7	—	—
Simulated					
Heterogeneous	$8.0 \times 10^{-6}$	$9.5 \times 10^{-5}$	10	2.5	200
620 nm					
Measured	$4.0 \times 10^{-4}$	$1.9 \times 10^{-2}$	22	—	—
Simulated					
Heterogeneous	$4.5 \times 10^{-4}$	$1.8 \times 10^{-2}$	25	1.6	32
Homogeneous: intestines <sup>a</sup>	$4.6 \times 10^{-4}$	$1.9 \times 10^{-2}$	26	0.5	29
Homogeneous: muscle <sup>a</sup>	$9.0 \times 10^{-4}$	$4.8 \times 10^{-2}$	30	0.5	98
640 nm					
Measured	$5.3 \times 10^{-4}$	$3.0 \times 10^{-2}$	28	—	—
Simulated					
Heterogeneous	$7.0 \times 10^{-4}$	$3.4 \times 10^{-2}$	28	0.5	42
Mouse 2: Traser in liver					
580 nm					
Measured	— <sup>b</sup>	— <sup>b</sup>	— <sup>b</sup>	—	—
Simulated					
Heterogeneous	$1.4 \times 10^{-8}$	$1.9 \times 10^{-8}$	4	—	—
620 nm					
Measured	$9.7 \times 10^{-5}$	$3.8 \times 10^{-3}$	17	—	—
Simulated					
Heterogeneous	$2.2 \times 10^{-5}$	$2.2 \times 10^{-3}$	28	0.9	150
Homogeneous: liver <sup>a</sup>	$1.4 \times 10^{-5}$	$1.2 \times 10^{-3}$	22	0.6	230
Homogeneous: muscle <sup>a</sup>	$1.0 \times 10^{-4}$	$1.6 \times 10^{-2}$	39	0.9	55
640 nm					
Measured	$1.6 \times 10^{-4}$	$7.2 \times 10^{-3}$	21	—	—
Simulated					
Heterogeneous	$5.3 \times 10^{-3}$	$3.6 \times 10^{-3}$	36	0.6	100
Mouse 3: Traser in intestines					
580 nm					

**Table 1** (Continued.)

Data set	Exitance		Spot Area (mm <sup>2</sup> )	Peak Distance (mm)	NRMS Difference (%)
	Peak (mm <sup>-2</sup> )	Total (—)			
Measured	$1.0 \times 10^{-4}$	$2.4 \times 10^{-3}$	18	—	—
Simulated					
Heterogeneous	$8.1 \times 10^{-6}$	$1.8 \times 10^{-4}$	21	1.0	340
620 nm					
Measured	$1.1 \times 10^{-3}$	$5.3 \times 10^{-2}$	25	—	—
Simulated					
Heterogeneous					
Center of Traser	$3.8 \times 10^{-4}$	$2.1 \times 10^{-2}$	36	1.0	95
Ventral end of Traser <sup>d</sup>	$1.3 \times 10^{-3}$	$4.3 \times 10^{-2}$	25	1.0	29
Dorsal end of Traser <sup>d</sup>	$1.6 \times 10^{-4}$	$1.1 \times 10^{-2}$	43	1.6	200
Extended source <sup>e</sup>	$6.1 \times 10^{-4}$	$2.5 \times 10^{-2}$	28	1.0	71
Center, $\mu_a$ reduced <sup>c</sup>	$6.3 \times 10^{-4}$	$3.6 \times 10^{-2}$	39	1.0	52
Homogeneous: intestines <sup>a</sup>	$2.9 \times 10^{-4}$	$1.1 \times 10^{-2}$	29	1.0	150
Homogeneous: muscle <sup>a</sup>	$6.1 \times 10^{-4}$	$3.1 \times 10^{-2}$	33	1.0	63
640 nm					
Measured	$1.3 \times 10^{-3}$	$7.3 \times 10^{-2}$	27	—	—
Simulated					
Heterogeneous	$6.1 \times 10^{-4}$	$3.5 \times 10^{-2}$	39	1.0	75

Peak exitance: peak intensity on skin, normalized to source power. Total exitance: integrated intensity on skin, normalized to source power. Spot area: area over which exitance exceeds half of peak value. Peak distance: distance between peak locations in measured and simulated images. NRMS difference: normalized root mean square difference between measured simulated and measured images.

<sup>a</sup>The optical properties of the given tissue were used in the homogeneous model.

<sup>b</sup>The exitance was too small to enable an accurate measurement.

<sup>c</sup>The absorption coefficient was reduced by 33% for every tissue.

<sup>d</sup>The source was moved in the ventral or dorsal directions by 1.2 mm (half the length of the Traser).

<sup>e</sup>Obtained by averaging the luminescence maps for the three source positions.

Figure 6 and Table 1 also show the simulated exitance data when the mouse body was assumed to be a single homogeneous medium. The results show that the measured exitance was, in all cases, in marginally worse agreement with the simulated exitance in the homogeneous case than in the heterogeneous case, when the properties of the homogeneous medium were taken to be those of the tissue in which the Traser was located. The difference between the heterogeneous and the homogeneous simulation was moderate, and in all cases smaller than the difference between the measured and the simulated data. Using muscle properties for the homogeneous medium, however, resulted in large changes in the simulated exitance and made the agreement with the measurement much worse.

In the Monte Carlo simulations, we used the reduced scattering coefficient and assumed isotropic scattering. It is, how-

ever, straightforward to implement anisotropic scattering in a Monte Carlo simulation. Although the anisotropy parameter  $g$  is not known for every tissue in the model, it is known that its value is quite high and that animal tissues are generally forward scattering.<sup>27,28</sup> To estimate how much of an error is made by assuming isotropic scattering, we have repeated the simulation on mouse 3 (at 620 nm) with  $g=0.9$  for all tissues; accordingly,  $\mu_s$  was multiplied by 10 to keep  $\mu'_s = \mu_s(1-g)$  unchanged. We found that the exitance patterns appeared to be essentially the same in the two cases, except that the exitance computed with  $g=0.9$  was systematically 10% lower. This number is approximately equal to the amount of energy lost by a photon at every scattering step, and is considered to be small and acceptable in this simulation. This confirms that, at the scale relevant to bioluminescence tomography, the an-

isotropy of the light scattering is inconsequential.<sup>35</sup>

## 5 Discussion

In the previous section, the discrepancy between the simulated and the measured bioluminescence images was quantified in terms of the differences in the peak exitance, total exitance, spot size and peak position, as well as with the NRMS difference. Generally, these numerical measures provide a good quantitative measure of the “difference” between the simulated and measured data, more so than a visual comparison between the 3-D exitance images. It is obvious, however, that global statistical measures of this difference, such as the NRMS difference, are of limited use, because their magnitude is determined mostly by small errors in the placement of the source. The cross-correlation of the measured and computed exitances is of no use here, because all the mesh triangles with zero exitance contribute to generate a very high number for it.

Ultimately, it is the discrepancy between the reconstructed BLI image and the true source distribution that will matter. This discrepancy will strongly depend on the details of the inverse algorithm: how many wavelengths are used simultaneously, what prior knowledge and assumptions are incorporated in the algorithm, what regularization function is used, etc. As the inverse problem in bioluminescence tomography is known to be underdetermined,<sup>37</sup> each of these factors can have a significant impact on the reconstructed image.

Going back to peak and total exitance and spot areas, we found significant differences between the simulated and measured data; a factor of 4 in the worst case. From our analysis, it seems reasonable to expect, in solving the forward problem in a general case, an error in the exitance of a factor of 2 or so. This discrepancy is expected to carry over to the reconstructed BLI images. Its impact would depend on the nature of the study in which the BLI images are used. For example, when tracking the exponential growth of a tumor, an error by a factor of 2 may not be important.

Still, the reasons for this discrepancy must be investigated further. The source of the error could be in any one or more of the following: the spatial map of the tissue optical properties, the position of the Traser, or the Monte Carlo algorithm itself. Since the general Monte Carlo algorithm (and the POLMC code itself, in particular) has been extensively tested, it is not a likely candidate. We chose instead to investigate, through more simulations, how a small change in the absorption coefficient of every tissue, or changes in the Traser position, affect the exitance patterns.

First, we repeated the simulation with the model for mouse 3, with which the largest overall discrepancy was obtained, but this time we decreased the absorption coefficient  $\mu_a$  by 33% for all tissues. Note that the magnitude of this change is much smaller than the variation in  $\mu_a$  between tissues, which is as large as a factor of 10. The results are presented in Table 1. The lower absorption brought the peak and total exitance more in line with the measured value, but the spot size in the simulation increased further away from the measured value, as is to be expected.

Second, we placed the source at either extremity of the Traser, which were found to be (in the MRI image) 1.2 mm away from the original source in the ventral and dorsal direc-

tions. Moving the source ventrally improved substantially the agreement between the measurement and the simulation, whereas moving it dorsally worsened it. Finally, we averaged the luminescence maps obtained with the source at the three positions, which is close to equivalent to the simulation of an extended source. This is the most realistic case, and it also improves the agreement. Overall, this demonstrates how sensitive the simulation is to small errors in source positioning, more so than to small errors in optical properties. Accordingly, how extended sources are handled in the calculation, even at the submillimeter scale, is expected to play a major role in its accuracy.

One of our initial objectives was to determine what error is incurred by ignoring the anatomy of the mouse, that is, by replacing the tissue map by a homogeneous medium in the simulation. It is obvious that using a single set of optical properties for sources located in different organs or tissues (as we did with muscle properties) causes large errors, by an order of magnitude or more. When the properties of the tissue in which the source is located are used, the agreement with the measured data is still worse than when the heterogeneous model is used. However, the additional error incurred is comparable to the original difference between the measured data and the data simulated with the heterogeneous model. We repeated the homogeneous simulation once more with the model of mouse 3 using three source positions and averaging, as we did with the heterogeneous model. The conclusion was the same: the agreement with the measured data improved substantially, but the data obtained from the heterogeneous model was still better.

Overall, the heterogeneous model is always superior to the homogeneous model, but only marginally so. In some cases, it may still be possible, though not as accurate, to carry out the bioluminescence image reconstruction with a homogeneous model, for example, when the source is confined to a region where the optical properties do not vary greatly between the tissues present, or when the tissue containing the source extends all the way to the skin.

## 6 Conclusions

We investigated how an anatomical model may be constructed from magnetic resonance images and incorporated in solving the forward problem (the propagation of light in tissue) in a live mouse. Our analysis was performed on three live mice in which tritium-powered artificial sources were surgically implanted. The model was successfully registered, with nonlinear transformations, to the 3-D exitance image. A direct and absolute comparison of the simulated and measured exitance images show differences ranging from a few percents to a factor of two or so. The main cause of the discrepancy was traced back to small errors in source placement and in the way by which extended sources were handled. A lesser part of the disagreement is likely due to inevitable errors in the optical properties (particularly in the absorption coefficient).

Our analysis reveals that a detailed anatomical model of the mouse marginally improves the accuracy of the simulated bioluminescence images and, by extension, should do so also for the reconstructed images. The improvement in the simulated images is not large enough to lead us to believe that bioluminescence tomography is impossible without this ana-

tomical model: it may be sufficient to know in which tissue the source is generally located. Having the anatomical model and a realistic list of optical properties is also not sufficient to eliminate the discrepancy between the simulated and measured exitance patterns. The way that extended sources are handled and the accuracy of the *a priori* knowledge of the optical properties of tissues in the mouse that is imaged will put an ultimate limit on the accuracy of forward-simulated images.

### Acknowledgments

We wish to thank Xenogen for their support. M. Allard acknowledges the support of the National Science and Engineering Research Council of Canada. R. M. Henkelman holds a Canada Research Chair in Imaging.

### References

1. R. Weissleder and V. Ntziachristos, "Shedding light onto live molecular targets," *Nat. Med.* **9**, 123–128 (2003).
2. T. F. Massoud and S. S. Gambhir, "Molecular imaging in living subjects: Seeing fundamental biological processes in a new light," *Genes Dev.* **17**, 545–580 (2003).
3. S. R. Cherry, "In vivo molecular and genomic imaging: New challenges for imaging physics," *Phys. Med. Biol.* **49**, R13–48 (2004).
4. C. H. Contag and B. D. Ross, "It's not just about anatomy: In vivo bioluminescence imaging as an eyepiece into biology," *J. Magn. Reson. Imaging* **16**, 378–387 (2002).
5. C. H. Contag and M. H. Bachmann, "Advances in *in vivo* bioluminescence imaging of gene expression," *Annu. Rev. Biomed. Eng.* **4**, 235–260 (2002).
6. J. Virostko, Z. Chen, M. Fowler, G. Poffenberger, A. C. Powers, and E. D. Jansen, "Factors influencing quantification of *in vivo* bioluminescence imaging: application to assessment of pancreatic islet transplants," *Mol. Imaging* **3**, 333–342 (2004).
7. X. Montet, V. Ntziachristos, J. Grimm, and R. Weissleder, "Tomographic fluorescence mapping of tumor targets," *Cancer Res.* **65**, 6330–6336 (2005).
8. Y. Xu, D. W. Piston, and C. H. Johnson, "A bioluminescence resonance energy transfer (BRET) system: application to interacting circadian clock protein," *Proc. Natl. Acad. Sci. U.S.A.* **96**, 151–156 (1999).
9. S. Y. Lee, Zh. Wang, C.-K. Lin, C. H. Contag, L. C. Olds, A. D. Coopers, and E. Sibley, "Regulation of intestine-specific spatiotemporal expression by the rat lactase promoter," *J. Biol. Chem.* **277**, 13099–13105 (2002).
10. D. E. Jenkins, S.-F. Yu, Y. S. Hornig, T. Purchio, and P. R. Contag, "In vivo monitoring of tumor relapse and metastasis using bioluminescent PC-3M-luc-C6 cells in murine models of human prostate cancer," *Clin. Exp. Metastasis* **20**, 745–756 (2003).
11. V. Ntziachristos, C. Bremer, and R. Weissleder, "Fluorescence imaging with near-infrared light: New technological advances that enable *in vivo* molecular imaging," *Eur. Radiol.* **13**, 195–208 (2003).
12. S. R. Arridge and J. C. Hebden, "Optical imaging in medicine: II. Modelling and reconstruction," *Phys. Med. Biol.* **42**, 841–853 (1997).
13. S. R. Arridge, "Optical tomography in medical imaging," *Inverse Probl.* **15**, R41–93 (1999).
14. H. Dehghani, B. W. Pogue, J. Shudong, B. Brooksby, and K. D. Paulsen, "Three-dimensional optical tomography: resolution in small-object imaging," *Appl. Opt.* **42**, 3117–3128 (2003).
15. C. Kuo, O. Coquoz, D. G. Stearns, and B. W. Rice, "Diffuse luminescence tomography of *in vivo* bioluminescent markers using multi-spectral data," *Proc. Soc. Molec. Imaging*, 180 (2004).
16. X. Gu, Q. Zhang, L. Lacom, and H. Jiang, "Three-dimensional bioluminescence tomography with model-based reconstruction," *Opt. Express* **12**, 3996–4000 (2004).
17. A. J. Chaudhari, F. Darvas, J. R. Bading, R. A. Moats, P. S. Conti, D. J. Smith, S. R. Cherry, and R. M. Leahy, "Hyperspectral and multi-spectral bioluminescence optical tomography for small animal imaging," *Phys. Med. Biol.* **50**, 5421–5441 (2005).
18. W. Cong, K. Durairaj, L. V. Wang, and G. Wang, "A Born-type approximation method for bioluminescence tomography," *Med. Phys.* **33**, 679–686 (2006).
19. A. X. Cong and G. Wang, "A finite-element-based reconstruction method for 3D fluorescence tomography," *Opt. Express* **13**, 9847–9857 (2005).
20. W. P. Segars, B. M. W. Tsui, E. Frey, G. A. Johnson, and S. S. Berr, "Development of a 4-D digital mouse phantom for molecular imaging research," *Molec. Imaging Biol.* **6**, 149–159 (2004).
21. C. Kuo, D. G. Stearns, and B. W. Rice, "Photon source localization and intensity quantification in diffuse luminescence tomography," in *Proc. OSA Biomedical Topical Meeting 2004*, p. 290 (2004).
22. B. C. Wilson and G. Adam, "A Monte Carlo model for the absorption and flux distributions of light in tissue," *Med. Phys.* **10**, 824–830 (1983).
23. H. Li, J. Tian, F. Zhu, W. Cong, L. V. Wang, E. A. Hoffman, and G. Wang, "A mouse optical simulation environment (mose) to investigate bioluminescent phenomena in the living mouse with the Monte Carlo method," *Acad. Radiol.* **11**, 1029–1038 (2004).
24. S. R. Arridge, M. Schweiger, M. Hiraoka, and D. T. Delpy, "A finite element approach for modeling photon transport in tissue," *Med. Phys.* **20**, 299–309 (1993).
25. M. Schweiger, S. R. Arridge, M. Hiraoka, and D. T. Delpy, "The finite element method for the propagation of light in scattering media: Boundary and source conditions," *Med. Phys.* **22**, 1779–1792 (1995).
26. B. C. Wilson and S. L. Jacques, "Optical reflectance and transmittance of tissues: principles and applications," *IEEE J. Quantum Electron.* **26**, 2186–2199 (1990).
27. W.-F. Cheong, S. A. Prahl, and A. J. Welch, "A review of the optical properties of biological tissues," *IEEE J. Quantum Electron.* **26**, 2166–2185 (1990).
28. V. Tuchin, *Tissue Optics*, SPIE Press, Bellingham, WA (2000).
29. F. Bevilacqua, D. Piguet, P. Marquet, J. D. Gross, B. J. Tromberg, and C. Depeursinge, "In vivo local determination of tissue optical properties: applications to human brain," *Appl. Opt.* **38**, 4939–4950 (1999).
30. G. Alexandrakis, F. R. Rannou, and A. F. Chaziiannou, "Tomographic bioluminescence imaging by use of a combined optical-PET (OPET) system: a computer simulation feasibility study," *Phys. Med. Biol.* **50**, 4225–4241 (2005).
31. H. Dehghani, S. C. Davis, S. Jiang, B. W. Pogue, K. D. Paulsen, and M. S. Patterson, "Spectrally resolved bioluminescence optical tomography," *Opt. Lett.* **31**, 365–367 (2006).
32. G. Alexandrakis, F. R. Rannou, and A. F. Chaziiannou, "Effect of optical property estimation accuracy on tomographic bioluminescence imaging: simulation of a combined optical-PET (OPET) system," *Phys. Med. Biol.* **51**, 2045–2053 (2006).
33. D. L. Collins, P. Neelin, T. M. Peters, and A. C. Evans, "Automatic 3D intersubject registration of MR volumetric data in standardized Talairach space," *J. Comput. Assist. Tomogr.* **18**, 192–205 (1994).
34. D. L. Collins, C. J. Holmes, T. M. Peters, and A. C. Evans, "Automatic 3-D model-based neuroanatomical segmentation," *Hum. Brain Mapp* **3**, 190–208 (1995).
35. F. Bevilacqua and C. Depeursinge, "Monte Carlo study of diffuse reflectance at source-detector separations close to one transport mean free path," *J. Opt. Soc. Am. A* **16**, 2935–2945 (1999).
36. D. Côté and I. A. Vitkin, "Robust concentration determination of optically active molecules in turbid media with validated three-dimensional polarization sensitive Monte Carlo calculations," *Opt. Express* **13**, 148–163 (2005).
37. G. Wang, Y. Li, and M. Jian, "Uniqueness theorems in bioluminescence imaging," *Med. Phys.* **31**, 2289–2299 (2004).